Journal of Materials Chemistry C

RSC Publishing

PAPER

View Article Online
View Journal | View Issue

Published on 25 March 2013. Downloaded by University of Wisconsin - Madison on 14/09/2016 17:08:48.

Cite this: *J. Mater. Chem. C*, 2013, **1**, 3110

Generation of scalable quasi-3D metallo-dielectric SERS substrates through orthogonal reactive ion etching†

Wonmi Ahn, Yue Qiu and Björn M. Reinhard*

We combined two orthogonal reactive ion etching strategies on monolayers of 4 μm diameter polystyrene (PS) microspheres assembled on a planar glass substrate to create geometrically diverse but highly regular quasi-3D nano-structured arrays with centimeter length scales. Reactive ion etching (RIE) with O_2/CF_4 was used to selectively etch PS and, thus, to adjust the morphology of the PS mask, and CHF_3 RIE was then used to etch the SiO_2 substrate. The dynamic combination of these two etching procedures facilitated the realization of a wide variety of 3D-corrugated surface morphologies, including pedestals, bowls, honeycombs and blossom bud like arrays. The generated structures were then evaporated with Au films of defined thicknesses to generate metallo-dielectric arrays with tunable surface roughness. Hexagonal diffraction patterns from the fabricated structures confirm the successful realization of extended periodic hexagonal structures and the optical transmission spectra showed an efficient trapping of incident light in these ultra-rough metallo-dielectric arrays. The metallo-dielectric substrates were finally optimized for the detection of the pesticide methyl parathion in a concentration as low as 1×10^{-10} M through surface enhanced Raman spectroscopy (SERS).

Received 17th January 2013
Accepted 21st March 2013

DOI: 10.1039/c3tc30110a

www.rsc.org/MaterialsC

Morphologically well-defined nanostructured noble metal surfaces are important components in near-field photonics,[1] plasmonic photovoltaics,[2] and plasmon enhanced chemical and biological sensing.[3,4] One prominent example of a plasmon enhanced spectroscopy is surface enhanced Raman spectroscopy (SERS).[5,6] While various nanofabrication methods have been applied to generate efficient SERS substrates that enhance the incident field by many orders of magnitude, many state-of-the-art nanofabrication approaches have only limited scalability, so that the economic fabrication of large-scale substrates still poses tremendous challenges. For example, electron beam lithography (EBL) and focused ion beam (FIB) can produce nanopatterns with feature sizes of a few nanometers, but they require expensive equipment and long writing times for areas of only few tens of μm^2. Alternative photolithographical techniques such as deep UV (DUV) lithography can pattern large areas in a relatively short period of time albeit with a reduced minimum feature size, which is on the order of a few tens of nanometers in DUV lithography. This reduction in resolution is accompanied by a reduction in electromagnetic field enhancement since small crevices and junctions are the locations of electromagnetic hot-spots, which dominate the electromagnetic part of the SERS signal enhancement.[7] Furthermore, DUV lithography still requires special equipment such as excimer lasers that might not be accessible in a typical laboratory environment or add significantly to the process costs.[8]

Self-assembly strategies have significant potential to overcome some of the shortcomings of conventional top-down nanofabrication. One facile fabrication approach for extended SERS substrates is based on the self-assembly of dielectric spheres of a defined diameter, which provides a regular corrugation of the refractive index.[9] This so-called nanosphere lithography (NSL) can be easily performed by controlling the rate of solvent evaporation to generate attractive capillary forces between colloidal spheres after spreading beads on supporting substrates by drop-,[10] dip-,[11] or spin-coating.[12,13] NSL can create regular arrays with lateral dimensions of millimeters or centimeters within a few minutes without the need for expensive lithography equipment.[14,15] Additional functionality can be achieved when these structures are converted into hybrid photonic–plasmonic structures by overcoating with a gold (Au) film. Metal films deposited over a monolayer of nano- or microspheres (metal film over colloidal crystal, MFoCC)[16–18] sustain both photonic and plasmonic resonances that can synergistically interact to create new capabilities that reach beyond those of the individual components. Depending on the periodicity and refractive index of the dielectric beads, the 2D array can transmit, scatter, reflect or laterally guide the normally incident light. Especially the coupling between laterally guided photonic modes in the dielectric component and propagating surface plasmon modes in the metal film of Au evaporated 2D arrays of dielectric beads has been investigated by

Department of Chemistry and The Photonics Center, Boston University, Boston, Massachusetts 02215, USA. E-mail: bmr@bu.edu

† Electronic supplementary information (ESI) available. See DOI: 10.1039/c3tc30110a

This journal is © The Royal Society of Chemistry 2013

Published on 25 March 2013. Downloaded by University of Wisconsin - Madison on 14/09/2016 17:08:48.

several groups to optimize extraordinary optical transmission (EOT) in these hybrid structures.[16,19–21]

The morphology of the NSL-based metallo-dielectric arrays can be conveniently modified through etching processes, which impart additional degrees of freedom to control metallic separations in the junction between the individual spheres and the roughness of the surface.[22,23] Wet[24]- and dry[25]-etching of the bead masks, angle resolved metal deposition,[14,26] and thermal annealing[27] have led to a wide variety of morphologically diverse metallic and metallo-dielectric hybrid nano-architectures for applications in SERS sensing,[28] split-ring resonator metamaterials,[26] high efficiency light-trapping solar cells,[29,30] and self-cleaning functional materials.[31] In particular, dry etching by reactive ion etching (RIE) has been adapted as an easy, versatile, and controllable method for shaping bead templates.[22,32,33] Different from isotropic wet etching processes, which are known to cause an undercutting on the substrate, RIE using reactive gases in high radio frequency EM fields is an anisotropic etch process that generates high-fidelity quasi-3D nano-patterns. Moreover, selective etching is possible in RIE because different RIE gasses are only reactive to specific materials. For example, fluorine containing gases are generally reactive to SiO_2 and oxygen etches polymeric organic materials such as polystyrene.[22,32,33] Therefore, RIE has been used as a convenient method to generate highly reproducible quasi-3D nano-patterns such as nano-pillars,[29,30] -disks,[34] -crescents,[26] -grails,[33] and -holes,[35] which are excellent candidates for potent SERS substrates.[28] However, a comprehensive study on the fine control of metallo-dielectric quasi-3D structures through subsequent orthogonal RIE is still missing. Moreover, existing RIE-generated SERS substrates increase the signal intensity only by roughening bead surfaces in 2D bead arrays. A potential gain in signal intensity in bead arrays on corrugated (quasi-3D) surfaces remains to be explored.

In this study we demonstrate that the complexity of NSL-based metallo-dielectric arrays can be further enhanced in a rational fashion by application of subsequent orthogonal RIE steps. We found that not only the number of RIE steps but also the density of beads in the NSL-generated pattern allow for a systematic tuning of the surface morphology. The aims of this manuscript are (1) to provide a systematic characterization of the relationship between the number of RIE steps and the pattern density on the morphology of the resulting substrate and (2) to characterize the performance of the metallo-dielectric arrays that result from overcoating with a Au layer of defined thicknesses. Finally, the performance of different RIE-generated metallo-dielectric arrays as SERS substrates will be benchmarked using the small molecule *para*-mercaptoaniline (*p*MA) and the pesticide methyl parathion.

Results and discussion

Multi-step patterning of metallo-dielectric arrays through nanosphere lithography and dry-etching

Fig. 1 outlines our fabrication strategy for regular quasi-3D metallo-dielectric arrays of high complexity on a planar glass substrate (see the Methods section for more details). The overall

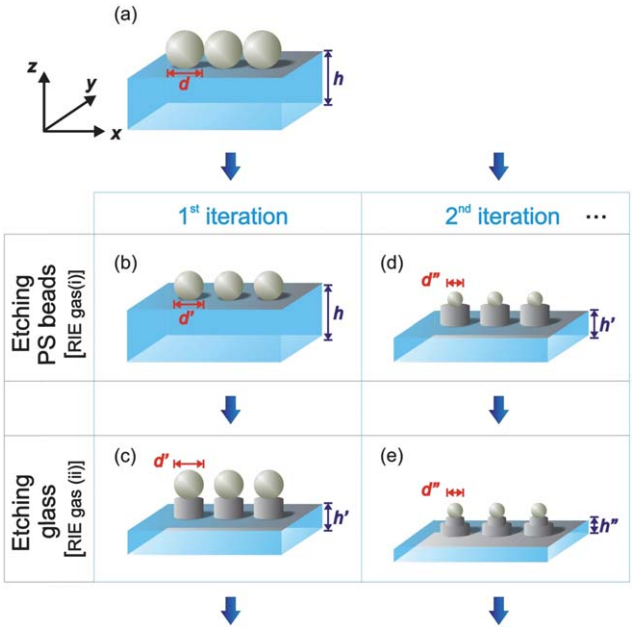

Fig. 1 Schematic illustration of the fabrication process for quasi-3D metallo-dielectric SERS substrates by orthogonal RIE on monolayers of PS beads. Two different RIE conditions were used to selectively etch PS beads or glass substrates: O_2/CF_4 [RIE gas (i)] or CH_3F [RIE gas (ii)], respectively. Consecutive RIE processes were performed up to 5 times to create diverse 3D nanostructures in hcp arrays of PS bead monolayers.

strategy of our fabrication approach is to combine two orthogonal etching procedures. The first one patterns the polystyrene (PS) bead mask and the second one removes the SiO_2 in all areas not protected by the mask. Through subsequent application of these two different etching steps we aim to generate a quasi-3D corrugated surface on which a Au film is evaporated to complete the metallo-dielectric structure.

In the first step of the fabrication (Fig. 1a) a defect-free monolayer of PS beads is formed on a 1×1 cm^2 glass substrate *via* convective self-assembly during the evaporation of the solvent in an environmental chamber that maintains constant temperature and humidity. In our set-up, the substrates were tilted at an angle of ~10°. The liquid evaporates faster at the top edge of the substrate, where the thinning of a PS bead droplet happens immediately after tilting the substrate, and slower at the bottom edge. When the water evaporates and the liquid film retracts across the surface from the raised end to the bottom of the substrate, the meniscus at the edge of the retracting liquid film has a force component perpendicular to the surface, which pushes the PS beads against the substrate. This force component ensures an efficient monolayer assembly. We found that the particle packing density of the bead monolayer on the slanted substrate is lower on the top of the substrate and higher on the bottom of the substrate (Fig. S1, ESI†). We attribute these differences in the particle packing density to a kinetic effect. The hexagonal close packed (hcp) monolayer only forms in areas where the aqueous PS bead dispersion dries slowly (bottom end, Fig. S1b†), whereas in areas of relatively fast meniscus migration (top end, Fig. S1a†) a regular monolayer with constant but larger bead-to-bead separation is obtained.

Published on 25 March 2013. Downloaded by University of Wisconsin - Madison on 14/09/2016 17:08:48.

After assembling the PS template a mixture of reactive gases, O_2/CF_4 [RIE gas (i)], is then used to decrease the average PS bead diameter (Fig. 1(b)). We used a flow rate of 17.3/29.7 sccm (standard cubic centimeters per minute) with a pressure of 16 mTorr and power of 20 W in this step of RIE. We found that under these conditions the PS beads are effectively etched and their diameter decreases linearly with etching time, while the supporting glass substrate is not affected. In a subsequent step (Fig. 1(c)) CHF_3 [RIE gas (ii)], which is mainly reactive to SiO_2, is used to etch down the glass substrate at 20 sccm, 16 mTorr, and 100 W. The selective etching of SiO_2 with [RIE gas (ii)] results in a patterning of the substrate along the *z*-axis, perpendicular to the plane of the bead array. We applied up to five consecutive etching steps (Fig. 1(d) and (e)) and obtained materials with high structural integrity and regularity even after application of long etching times of up to 2 h. A decrease of a polystyrene bead diameter (*d*) was only affected by etching with [RIE gas (i)] and a thickness of the glass substrate (*h*) was changed by [RIE gas (ii)]. After the completion of the etching procedure, we deposited thin layers of Cr/Au (5/40 nm) on these templates before the samples were transferred for inspection into the scanning electron microscope (SEM).

Fig. 2 provides an overview of the array morphology as functions of the three different experimental parameters: (1) RIE time using either [RIE gas (i)] O_2/CF_4 or [RIE gas (ii)] CHF_3, (2) the number of RIE steps, and (3) the packing density of the PS bead monolayer. The samples prepared by each RIE gas were designated by the symbol, $RIE_{t_2}^{t_1}$, where t_1 and t_2 indicate the RIE time in min performed with RIE gas (i) and (ii), respectively. The varied RIE times, *t*, are written on each SEM image. Two t_1 times separated by a "+" indicate two RIE steps with [RIE gas (i)] separated by one RIE step with [RIE gas (ii)].

The RIE step (I) in Fig. 2 was performed only with the [RIE gas (i)] on a hcp PS bead monolayer. The average PS bead diameter reduced from 3.5 μm (a), over 2.8 μm (b), to 2.3 μm (c) as the RIE time was increased from $t = 30$ min (a), over $t = 40$ min (b), to $t = 50$ min (c). The SEM images also confirm that the top surface of the PS beads became rougher when the beads were etched for a longer time. Fig. 3 shows the same arrays as in Fig. 2 after removal of the PS beads using a small piece of Kapton polyimide tape, and Fig. S2† contains their SEM images acquired with a tilt angle of 25°. Fig. 3I and S2I† clearly confirms that under the chosen experimental conditions [RIE gas (i)] selectively etches the PS beads but not the supporting glass substrate. After RIE step (I) only traces of PS deposited in circular rings were observed without any indications of an etching into the substrate.

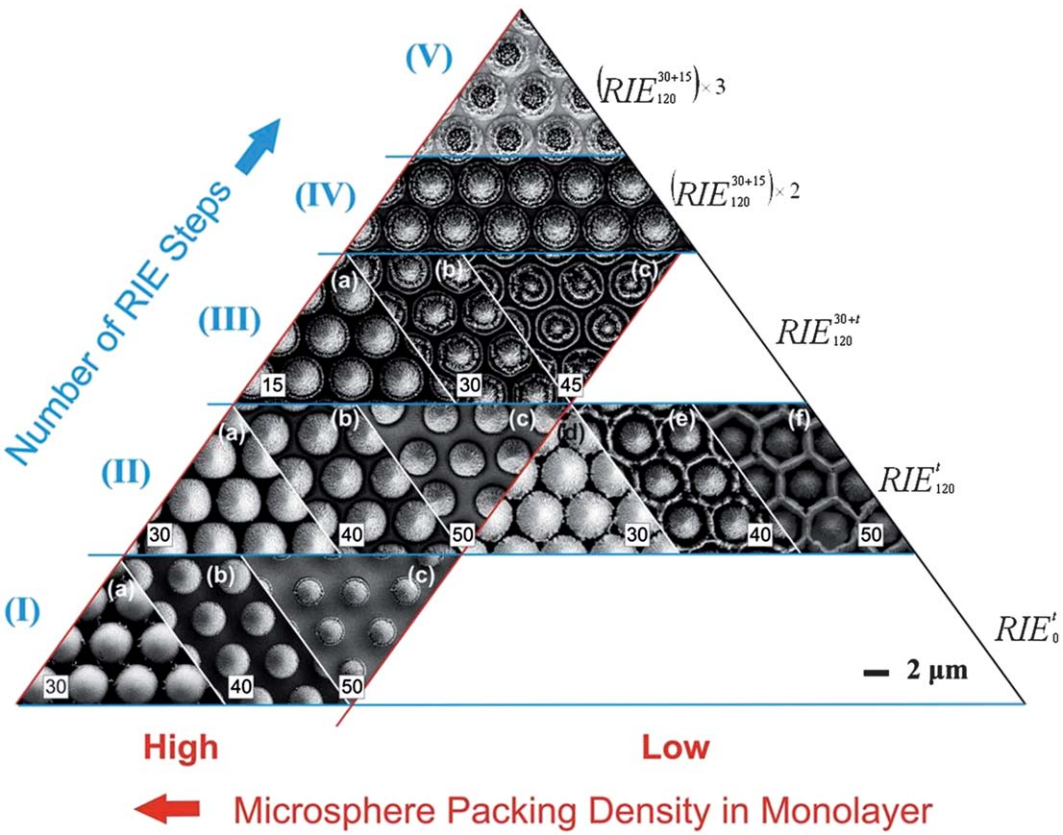

Fig. 2 Ternary diagram summarizing the morphology of quasi-3D metallo-dielectric arrays as functions of three main experimental variables: (1) number and sequence of RIE steps, (2) RIE time (provided as insets in the SEM images), and (3) particle packing density in PS monolayers. The details of the RIE process are given by the symbol, $RIE_{t_2}^{t_1}$, where t_1 and t_2 are RIE time performed with RIE gas (i) and (ii), respectively. Two t_1 times separated by a "+" indicate two RIE steps with [RIE gas (i)] separated by one RIE step with [RIE gas (ii)].

 This journal is © The Royal Society of Chemistry 2013

Published on 25 March 2013. Downloaded by University of Wisconsin - Madison on 14/09/2016 17:08:48.

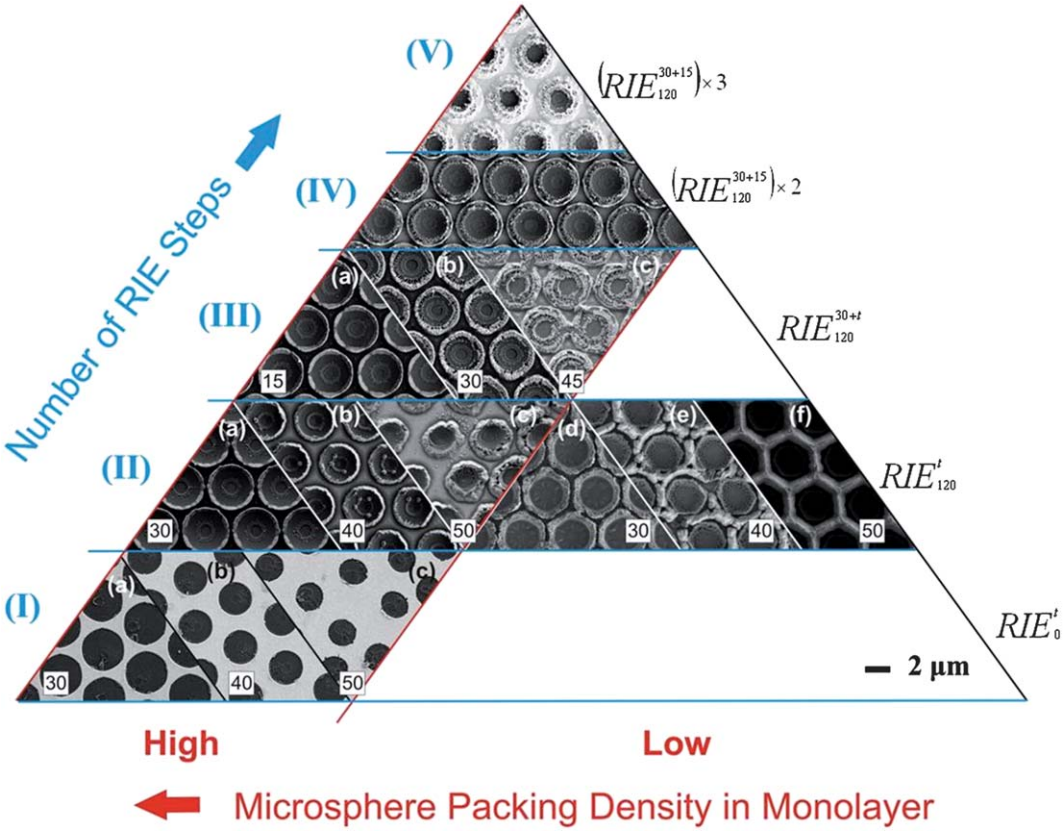

Fig. 3 Ternary diagram of quasi-3D metallo-dielectric arrays analogous to Fig. 2 but after removal of PS beads.

RIE step (II) was consecutively applied to the etched bead templates prepared in the RIE step (I), resulting in the structures shown in Fig. 2II(a)–(c), respectively. We applied [RIE gas (ii)] for 120 min to carve down the exposed areas of the glass substrate. The SEM images in Fig. 2II confirm the good homogeneity of the array; the fluctuations in the bead diameters are less than 4%. We again removed the etched beads and released regular arrays of concave bowl-looking nanostructures in Fig. 3II(a)–(c) and S2II(a)–(c)† at the locations of the original beads. Due to the glass etching through [RIE gas (ii)] the concave bowl structures are now raised in height and located on pedestals. The SEM images show that for these inverse structures Au deposition is restricted to the sharp edges (a) and outer walls (b and c) of the nanobowls. The bowls in (b and c) have more blunt edges than the ones in (a), due to a more efficient etching on the outer walls for larger interbead gaps. Circular marks of PS residues were left in the center of each bowl because plasma reaction by-products were deposited simultaneously with glass substrate etching. Bowl diameters were determined as 3.6 μm (a), 2.9 μm (b), and 2.4 μm (c), respectively.

We observed the formation of honeycomb structures when [RIE gas (ii)] was applied for 120 min to the loosely packed hcp monolayers of PS beads found in the areas of rapid liquid film retraction in Fig. 2II(d)–(f). The rigid honeycomb walls formed as the etching time during RIE step (I) was increased from $t = 30$ min (d), over $t = 40$ min (e), to $t = 50$ min (f), respectively. Energy-dispersive X-ray spectroscopy (EDAX) composition analysis (Fig. S3†) revealed that these honeycomb walls were made of PS, which is mostly composed of carbon. As the gap sizes between the etched beads were increased more rigid honeycomb walls were formed. We attribute the formation of the honeycomb structures to a redeposition of PS onto substrate areas located between the beads during RIE step (I). This is an important observation since it demonstrates that the etching of the PS beads impact the template mask not only by reducing the PS bead diameter but also through a re-deposition of PS. The deposition of PS in regular patterns on the substrate provides additional degrees of freedom to shape the array morphology in a systematic fashion. When the etched PS beads were removed, glass nanobowls with concave tops were exposed inside of the Au film-coated PS honeycomb walls as shown in Fig. 3II and S2(d–f).† These fascinating artificial hexagonal structures mimic natural honeycombs on the μm length scale and have potential applications as photonic crystal components, micro-volume channels for lab-on-a-chip devices, and confined isolated chemical reaction chambers.

We performed an additional RIE step (III) using [RIE gas (i)] to further reduce the size of PS beads, which resulted in concentric Au rings with variable widths on the top of the glass pedestals. The diameters of the PS beads (Fig. 2III and 3III) were decreased from 2.9 μm (a), over 2.0 μm (b), to 1.0 μm (c) on the glass pedestals for etching times $t = 15$, 30, and 45 min, respectively. The roughness of the PS beads was increased over etching time. Consistent with the decrease in bead size, we

Published on 25 March 2013. Downloaded by University of Wisconsin - Madison on 14/09/2016 17:08:48.

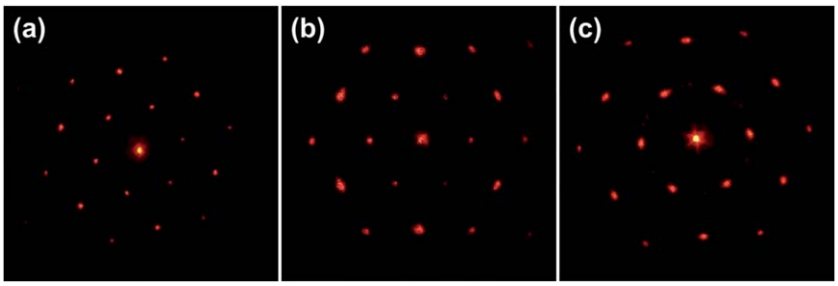

Fig. 4 Selected laser diffraction patterns of quasi-3D metallo-dielectric arrays. The patterns correspond (from left to right) to the arrays shown in Fig. 2 (a) II-a, (b) III-a and (c) V, respectively.

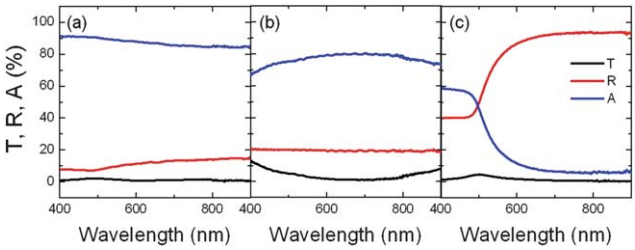

Fig. 5 Transmission (*T*), reflectance (*R*), and absorption (*A*) spectra of patterned arrays after (a) and (b) before deposition of a 60 nm thin Au film on the array configuration shown in Fig. 2III(a). (c) Reference spectra of a 60 nm thick Au film on a non-patterned glass substrate. All spectra were recorded at normal incidence using non-polarized light.

found that – after deposition of the Au film and removal of the beads – the widths of the Au rings on the SiO_2 pedestals increased from 270.9 nm (a), over 384.0 nm (b), to 648.3 nm (c). The bottom of the nanobowls revealed entirely Au-free surfaces in Fig. 3III and S2III(a)–(c).†

Even more complicated nanopatterns were created through application of additional RIE steps. In Fig. 2IV and V, RIE etching using [RIE gas (i) and (ii)] was repeated twice and three times more, respectively. The etched beads in Fig. 2IV are located on top of a pedestal in the centre of two concentric nanostructured Au ring (Fig. 3IV and S2IV†). Three subsequent RIE steps resulted in even smaller PS beads located in nanobowls on top of concentric pedestals with multiple height steps as shown in Fig. 2V, 3V and S2V.† The smooth outer surface of the original PS beads was completely transformed into ultra-rough blossom bud looking particles. These nano-architectures, which contain rough Au nanoparticle rings, nanobowls, and blossom bud like particles, are robust platforms for applications in biology and materials science that require rough quasi-3D surfaces with tunable morphologies. One particular advantage of the implemented fabrication strategy is that it also facilitates the formation of high aspect ratio negative curvature surface features, which are difficult to produce with other fabrication techniques, simply through removal of the beads. Furthermore, the removal of beads has been shown to increase the sensitivity for localized surface plasmon resonance (LSPR) sensing in non-etched metalized bead arrays.[36] The demonstrated ability to create a broad range of positive and negative surface features illustrates the versatility of our fabrication approach. While we focus on the positive curvature surface features in this manuscript, the negative surface features have important potential applications such as ultra hydrophobic surfaces, isolated micro-channels, and efficient optofluidic chips.

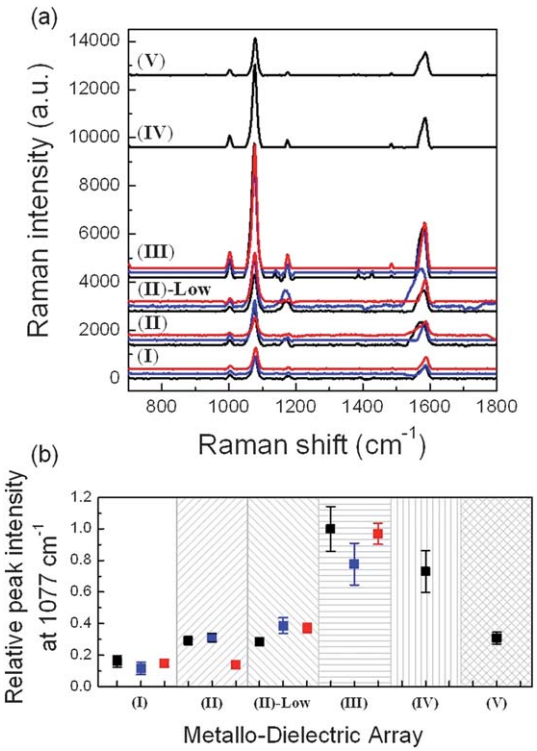

Fig. 6 (a) SERS spectra of *p*MA molecules (100 μM in ethanol) chemisorbed on metallo-dielectric arrays as shown in Fig. 2. Black, blue, and red lines correspond to samples with identical number of etching steps but increasing duration of etching in the last step. (b) SERS intensities of the 1077 cm^{-1} stretch mode averaged over 5 different measurements on each array sample. Standard deviations are included as error bars.

Laser diffraction patterns validate the large-scale integrity and periodicity of metallo-dielectric arrays

In addition to characterizing the morphologies of the fabricated arrays through SEM, we also performed laser diffraction

 This journal is © The Royal Society of Chemistry 2013

Published on 25 March 2013. Downloaded by University of Wisconsin - Madison on 14/09/2016 17:08:48.

experiments to validate the integrity and periodicity of the structures. Fig. 4(a)–(c) show diffraction patterns obtained with a 632.8 nm laser (beam size of 1.5 mm) from the nanopatterns shown in Fig. 2II(a), III(a) and V, respectively. The diffraction patterns of the arrays show distinct hexagonal diffraction spots indicating defect-free regular structures over large domain sizes, even in cases that involve multiple try etching steps (Fig. 4(c)). We obtained uniform diffraction patterns at locations separated by several millimeters. This observation confirms that the resulted metallo-dielectric arrays exhibit a high degree of regularity over macroscopic length scales.

Optical transmission, reflectance, and absorption measurements

The optical transmission (T) and reflectance (R) spectra in the spectral range between 400 and 900 nm are shown in Fig. 5 for the array configuration shown in Fig. 2III(a). The spectra were obtained using a UV-vis spectrometer at normal incidence of non-polarized light with (a) and without (b) deposition of a 60 nm thin Au film. In Fig. 5(c) we show the corresponding spectra for a 60 nm thin Au film on a planar SiO_2 substrate. While the control Au film shows low transmission but a high reflectance for $\lambda > 500$ nm (*i.e.* energies below the interband transition), the nanopatterned arrays in Fig. 5(a) and (b) show both a low reflectance and transmission across the entire spectral range. This observation indicates an efficient trapping of incident light in the plane of the array. Interestingly, both transmission and reflectance in the metallo-dielectric array are lower than in the dielectric array, which is consistent with additional light absorption in the hybrid structure across the investigated wavelength range due to excitation of plasmons. Light that is incident onto the corrugated metallo-dielectric surface is re-radiated into the array plane where it can excite both localized surface plasmons and propagating Bragg-like plasmon modes.[16,20,37,38] The excited plasmons can then interact with the photonic eigenmodes of the PS bead monolayer to form delocalized photonic–plasmonic hybrid modes. The trapping of light in standing waves confined to the plane of the metallo-dielectric array has obvious parallels with light trapping through another interference phenomenon, slow light,[39] which has also been shown to induce efficient light localization in grated metal films[40] and metallo-dielectric[41] waveguides.

Characterization of SERS performance of metallo-dielectric arrays

In the next step we compared the SERS signal intensities obtained for the different metallo-dielectric arrays summarized in Fig. 2. We first characterized the influence of the array morphology on the SERS signal intensity while we kept the thickness of the Au layer constant (40 nm). We used *para*-mercaptoaniline (*p*MA) for these benchmarking experiments since it readily chemisorbs onto Au surfaces. The samples were incubated in a 100 μM solution of *p*MA in ethanol for 30 min, subsequently rinsed with copious amounts of fresh ethanol, and then dried in a stream of nitrogen gas. Then, we acquired SERS spectra of the samples in air with a homebuilt Raman microscope using a 785 nm laser diode as excitation source (see Methods). We averaged the SERS signal over an area of 1.8×8.6 μm^2 and all spectra were background corrected by subtraction of a spectrum recorded from an adjacent area on the substrate that did not contain any nanostructured features. Fig. 6(a) summarizes representative SERS spectra for the quasi-3D arrays

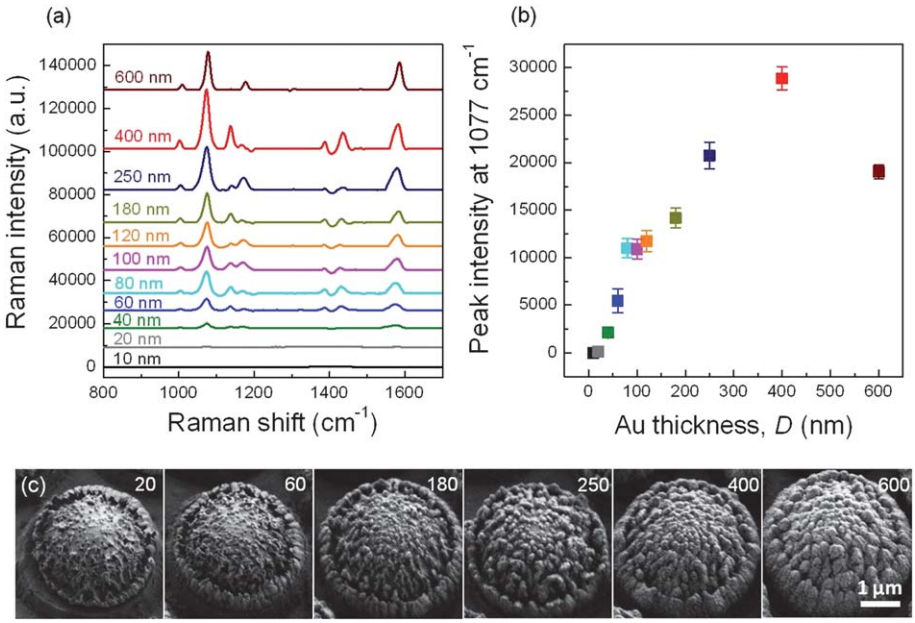

Fig. 7 (a) SERS spectra of *p*MA molecules chemisorbed on array (III)-a (see Fig. 2) with different Au films thicknesses (D) ranging from 10 to 600 nm. (b) Peak SERS intensities for the 1077 cm^{-1} band as function of D. The plotted values are averages over 5 measurements on one chip; standard deviations are included as error bars. (c) 25° tilted SEM images of the RIE-generated dielectric microspheres for D values as indicated.

Published on 25 March 2013. Downloaded by University of Wisconsin - Madison on 14/09/2016 17:08:48.

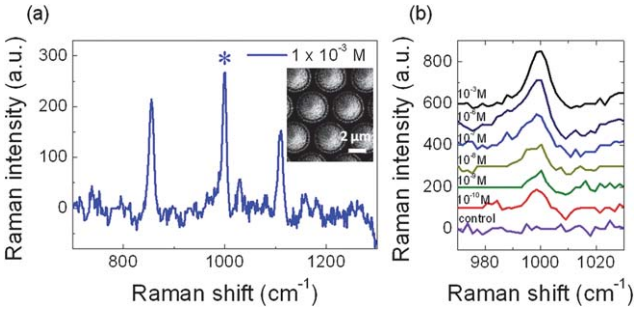

Fig. 8 (a) Representative SERS spectrum of methyl parathion (1×10^{-3} M in ethanol) obtained with array (III)-a (see Fig. 2 and inset SEM. Scale bar is 2 μm). (b) Peak intensity of the 1003 cm^{-1} band obtained on the array (III)-a for methyl-parathion concentrations ranging between 1×10^{-3} M and 1×10^{-10} M (top to bottom). The SERS spectrum of an array without methyl parathion was included as control.

shown in Fig. 2. The etching times for the nanopatterns were increased from black, blue, to red lines in the designated RIE step from (I) to (V). Each spectrum is an average of SERS measurements from at least five different areas. The *p*MA peaks at 1077 cm^{-1} (C–S stretch) and 1583 cm^{-1} (C–C stretch), 1003 cm^{-1} (C–C stretch), and 1174 cm^{-1} (C–H bend) continuously increase going from (I) to (III) but then drop again for (IV) and (V). Fig. 6(b) contains the average SERS peak intensity of the 1077 cm^{-1} C–S stretch mode for all investigated metallo-dielectric arrays. The standard deviation of the SERS signal intensity obtained for measurements at random locations of the investigated arrays is included as error bars and provides a measure of the lateral fluctuation in the SERS signal amplification for the investigated samples. The minimum coefficient of variation of the SERS signal intensity for the substrate in Fig. 6 was 4% and the signal from independently generated substrates exhibited typical coefficients of variations on the order of 13%. These results confirm that our easy and cost-effective method for generating metallo-dielectric arrays achieve excellent on-chip and good chip-to-chip SERS signal reproducibilities. One striking feature in Fig. 6(b) is the significant SERS signal intensity increase by almost an order of magnitude upon application of the second PS bead etching step through [RIE gas (i)] in array (III). As can be seen from the SEM images in Fig. 2III, this additional round of etching significantly intensifies the nanoscale roughness, and this increase in nanoscale roughness is consistent with a higher SERS signal enhancement. Application of additional rounds of RIE etching with both [RIE gas (i) and (ii)] reduced, however, the signal intensity observed for arrays (IV) and especially (V).

The signal intensity of array (V) dropped to the same level observed for arrays (II). Overall, these observations indicate that although RIE increases the surface roughness and, thus, accounts for the observed difference in SERS signal intensity between arrays (I and II) and (III), it also reduces the size of the PS beads that define the array. All fabricated metallo-dielectric arrays show broad plasmon resonance bands that overlap with the SERS pump and emission wavelengths (Fig. 5). We, consequently, attribute the reduction in SERS signal intensity between (III) and (IV and V) primarily to the decrease in total roughened surface area as the bead diameter is reduced through repeated RIE.

After characterizing the influence of RIE generated surface morphology on the SERS signal, we set out to identify the ideal Au coating thickness to boost the SERS signal intensity. We used the nanostructure array shown in Fig. 2III(a) for this experiment and systematically varied the Au thickness, D, between 10 and 600 nm. We found that the SERS signal intensity increases with growing D up to $D = 400$ nm, where the signal intensity becomes maximum (Fig. 7(a) and (b)). At $D = 600$ nm the SERS signal decreases to the value measured for $D = 250$ nm. The chosen array configuration (III)-a contains etched beads on sharply edged bowl-like pedestals and shows a high degree of roughness after repeated [RIE gas (i) and (ii)] treatment. We included SEM images of individual metalized etched beads for array (III)-a after evaporation of a Au film with nominal thickness of $D = 20$–600 nm (Fig. 7c). The SEM image for $D = 20$ nm shows a thin Au meshwork with sharp, nanoscale features over a rough PS surface. With increasing D these Au features coalesce into all-metal Au rods that protrude from the PS surface. The formation of larger Au structures that can sustain stronger E-field enhancement[3] is consistent with the increase in SERS signal intensity up to $D = 400$ nm. Our measurements indicate, however, that for even thicker Au layers (*i.e.* $D = 600$ nm) increased absorption (data not shown) and dissipative losses in the Au film result in a decrease in SERS signal intensity.

For most analytical application the most important figure of merit of any SERS substrate is the detection limit for a specific target analyte. We tested the performance of optimized metallo-dielectric arrays for the detection of ultra-low levels of methyl parathion molecules, which is a widely used insecticide.[42] The detection limits of methyl parathion using gas chromatography coupled with electron capture (GC-ECD) are 0.1 μg L^{-1} in water and 0.01 mg kg^{-1} in plant tissues.[43] It has been demonstrated, before, that SERS allows to significantly improve this detection limit for methyl parathion,[44,45] which made methyl parathion an interesting analyte to benchmark the SERS performance of optimized metallo-dielectric arrays. We again used the array configuration (III)-a and chose – as compromise between performance and price – an Au layer of $D = 180$ nm in these experiments. The prepared nanostructures were incubated in different concentrations of methyl parathion solutions ranging from 1×10^{-10} to 1×10^{-3} M dissolved in ethanol for overnight, rinsed with fresh ethanol, and dried with a stream of N_2.

Fig. 8(a) shows typical SERS spectrum of methyl parathion obtained with an analyte concentration of 1×10^{-3} M. The major methyl parathion peaks at 851 cm^{-1} (P–O stretch), 1003 cm^{-1} (C–O stretch), and 1132 cm^{-1} (C–N stretch) are significantly enhanced on the rough surface of metallo-dielectric arrays. To determine the detection limit of methyl parathion on the metallo-dielectric array, we analyzed the change in intensity of the characteristic C–O stretch band as function of methyl parathion concentration. The results shown in Fig. 8(b) confirm that optimized metallo-dielectric arrays can detect the C–O stretch band down to methyl parathion concentration of 1×10^{-10} M. This strong signal enhancement was homogeneously

 This journal is © The Royal Society of Chemistry 2013

Published on 25 March 2013. Downloaded by University of Wisconsin - Madison on 14/09/2016 17:08:48.

observed across the entire prepared metallo-dielectric array surface and did not require the use of additional methyl parathion capture and enrichment mechanisms used in previous studies.[45] Overall, these findings confirm that the fabricated metallo-dielectric arrays are versatile substrates for ultrasensitive SERS analytics.

Conclusion

We have investigated the morphological variability in quasi-3D metallo-dielectric arrays fabricated through a combination of orthogonal RIE processes and subsequent Au evaporation on NSL generated PS bead masks. Adjustment of the etching parameters, including the chemical composition of the RIE gas, gas flow rate, pressure, and power of the RIE chamber facilitated the fabrication of intricate surface morphologies through selective etching of PS beads or glass substrate. We demonstrated that orthogonal RIE is an economic approach for fabricating macroscopic areas of complex morphologies, including pedestals, bowls, and blossom bud like structures. We also demonstrated that etching conditions can be found so that the re-deposition of PS on the substrate results in the formation of extended networks of honeycomb structures. Au deposition transformed all of these structured surfaces into metallo-dielectric hybrid arrays that provide high SERS signal enhancements. Optimized arrays allowed the detection of the insecticide methyl parathion at concentrations as low as 1×10^{-10} M, which clearly emphasizes the value of these materials as substrates in surface enhanced spectroscopies. We conclude that metallo-dielectric arrays represent scalable substrates for a broad range of applications that require rough quasi-3D surfaces with tunable morphologies.

Methods

Substrate pre-treatment

Glass substrates (1×1 cm^2; Fisher Scientific Inc.) were cleaned in a 120 °C piranha solution (concentrated H_2SO_4/30% H_2O_2 = 3 : 1 vol.; **warning**: piranha solution is potentially explosive and can cause skin burns) for 30 min to remove organic matters and to hydroxylate the substrate surface. After cooling, piranha solution was rinsed from the substrates with copious amounts of water. Substrates were then sonicated in a fresh mixture of H_2O : NH_4OH : 30% H_2O_2 (5 : 1 : 1 vol.) for 60 min to make the surface more hydrophilic. After rinsing with water, substrates were stored in clean distilled water until use.

Polystyrene bead monolayer formation

The PS bead monolayer was formed by placing 40–50 μL of 0.37% PS bead suspension (4.00 ± 0.04 μm in diameter; Thermo Fisher Scientific) on these hydroxylated substrates. We found PS beads self-assemble into a close-packed monolayer with higher quality when substrates are placed in a closed environmental chamber at a constant relative humidity (RH < 2%), temperature ($T = 25$ °C), and pressure ($P = 0.9$ atm) with a tilt angle ~10°. Monolayer formation of PS beads was started from the top area of the substrate where water evaporation takes place first and resulting water flux drags beads upwards.

Reactive ion etching (RIE) on PS bead monolayer substrates

The anisotropic dry etching process consisted of two steps using (i) a mixture of reactive gases of O_2/CF_4 (17.3/29.7 sccm, standard cubic centimeters per minute) at a pressure of 16 mTorr and a power of 20 W to reduce the size of the PS beads, and (ii) CHF_3 (20 sccm) only at 16 mTorr and 100 W to etch down the glass substrate. Etching times and repetitive etching steps were varied for individual pattern formation (indicated in Fig. 2). A RIE chamber was pre-run with a gas or gas mixture of the next run for 10 min to ensure reproducible etching results.

Metal deposition and bead removal

A Cr/Au layer with a thickness of 5/40 nm (deposition rates of 0.5/1.0 Å s^{-1}), respectively, was then deposited on each final substrate of the etched colloidal templates by electron beam evaporation (CHA Industries) to create metallo-dielectric arrays. The etched polystyrene beads were easily removed by applying a small piece of Kapton polyimide tape on the substrate without breaking array regularity.

Characterization *via* SEM, UV-vis spectrometry, and laser diffraction pattern

Scanning electron microscopy (SUPRA 40VP, Zeiss) was used to characterize the microscopic morphologies of the metallo-dielectric regular arrays with 1–1.5 kV electron beam. Light transmission spectra of the sample were measured using a UV/VIS/NIR spectrophotometer (Cary 5000, Varian/Agilent) in a 400–900 nm wavelength range. A sample holder with a circular slit diameter of 1 mm was used to record data under normal incidence of unpolarized light. A blank glass substrate was used to obtain reference spectra. The high regularity on the fabricated nanopatterned arrays was verified by laser diffraction pattern measurement using a He–Ne laser ($\lambda = 632.8$ nm; a spot size of 1.5 mm) illuminating at a normal incident angle to the substrate. The diffraction patterns were projected on the collecting screen and captured using a digital camera.

SERS measurements of *para*-mercaptoaniline (*p*MA) and methyl parathion on metallo-dielectric arrays

The metallo-dielectric arrays were immersed in *p*MA solution (100 μM dissolved in ethanol) for 30 min. For detection of methyl parathion, a wide range of concentrations of methyl parathion solutions (1×10^{-3} to 1×10^{-10} M) were prepared in ethanol and the metallo-dielectric arrays were immersed in each solution for overnight. After incubation substrates were washed with fresh ethanol and then dried with a stream of N_2 gas. An upright Olympus BX51W1 microscope equipped with a 300 mm focal length imaging spectrometer (Andor Shamrock 303i) was used for SERS measurements. A 785 nm laser diode served as excitation source with a power of approximately 30 mW. The SERS signal was collected by a 40× objective (N.A. 0.65) from an active area confined by a mechanical slit

Published on 25 March 2013. Downloaded by University of Wisconsin - Madison on 14/09/2016 17:08:48.

($1.8 \times 8.6\ \mu m^2$). Average SERS signals were collected by taking SERS spectra from 5–10 different areas on the prepared metallo-dielectric array. The obtained SERS spectra were background corrected by subtracting SERS signals obtained from the adjacent area void of etched beads. Then the background corrected signals were baseline corrected using a peak analyzer function in OriginPro 8.5.

Acknowledgements

This work was financially supported by the National Science Foundation through grants CBET-1159552 and CBET-0953121.

References

1 A. V. Zayats and I. I. Smolyaninov, *J. Opt. A: Pure Appl. Opt.*, 2003, **5**, S16.
2 H. A. Atwater and A. Polman, *Nat. Mater.*, 2010, **9**, 205.
3 B. Yan, S. V. Boriskina and B. M. Reinhard, *J. Phys. Chem. C*, 2011, **115**, 24437.
4 W. Ahn, S. V. Boriskina, Y. Hong and B. M. Reinhard, *Nano Lett.*, 2012, **12**, 219.
5 B. Sharma, R. R. Frontiera, A.-I. Henry, E. Ringe and R. P. Van Duyne, *Mater. Today*, 2012, **15**, 16.
6 B. Saute and R. Narayanan, *Analyst*, 2011, **136**, 527.
7 C. E. Talley, J. B. Jackson, C. Oubre, N. K. Grady, C. W. Hollars, S. M. Lane, T. R. Huser, P. Nordlander and N. J. Halas, *Nano Lett.*, 2005, **5**, 1569.
8 W.-J. Fischer and M. Mertig, Bio and Nano Packaging Techniques for Electron Devices – Advances in Electronic Device Packaging, in *Nanopatterning and self-assembly in Microsystems: An overview*, Springer, 2012, ch. 9.
9 S. G. Romanov, A. V. Korovin, A. Regensburger and U. Peschel, *Adv. Mater.*, 2011, **23**, 2515.
10 N. D. Denkov, O. D. Velve, P. A. Kralchevsky, I. B. Ivanov, H. Yoshimura and K. Nagayama, *Langmuir*, 1992, **8**, 3183.
11 S. Takeda and P. Wiltzius, *Chem. Mater.*, 2006, **18**, 5643.
12 A. Mihi, M. Ocana and H. Miguez, *Adv. Mater.*, 2006, **18**, 2244.
13 P. Jiang and M. J. McFarland, *J. Am. Chem. Soc.*, 2004, **126**, 13778.
14 C. L. Haynes and R. P. Van Duyne, *J. Phys. Chem. B*, 2001, **105**, 5599.
15 W. Ahn and D. K. Roper, *ACS Nano*, 2010, **4**, 4181.
16 C. Farcau, M. Giloan, E. Vinteler and S. Astilean, *Appl. Phys. B: Lasers Opt.*, 2012, **106**, 849.
17 M. Lopez-Garcia, J. F. Galisteo-Lopez, A. Blanco, C. Lopez and A. Garcia-Martin, *Adv. Funct. Mater.*, 2010, **20**, 4338.
18 O. Benson, *Nature*, 2011, **480**, 193.
19 P. Zhan, J. B. Liu, W. Dong, H. Dong, Z. Chen, Z. L. Wang, Y. Zhang, S. N. Zhu and N. B. Ming, *Appl. Phys. Lett.*, 2005, **86**, 051108.
20 Z. Liu, J. Hang, J. Chen, Z. Yan, C. Tang, Z. Chen and P. Zhan, *Opt. Express*, 2012, **20**, 9215.
21 L. Landström, D. Brodoceanu, D. Bäuerle, F. J. Garcia-Vidal, S. G. Rodrigo and L. Martin-Moreno, *Opt. Express*, 2009, **17**, 761.
22 B. J.-Y. Tan, C.-H. Sow, K.-Y. Lim, F.-C. Cheong, G.-L. Chong, A. T.-S. Wee and C.-K. Ong, *J. Phys. Chem. B*, 2004, **108**, 18575.
23 L. Li, T. Zhai, H. Zeng, X. Fang, Y. Bando and D. Golberg, *J. Mater. Chem.*, 2011, **21**, 40.
24 T. Asefa and Y.-L. Shi, *J. Mater. Chem.*, 2008, **18**, 5604.
25 C. L. Cheung, R. J. Nikolić, C. E. Reinhardt and T. F. Wang, *Nanotechnology*, 2006, **17**, 1339.
26 M. C. Gwinner, E. Koroknay, L. Fu, P. Patoka, W. Kandulski, M. Giersig and H. Giessen, *Small*, 2009, **5**, 400.
27 A. Kosiorek, W. Kandulski, H. Glaczynska and M. Giersig, *Small*, 2005, **1**, 439.
28 H.-Y. Hsieh, J.-L. Xiao, C.-H. Lee, T.-W. Huang, C.-S. Yang, P.-C. Wang and F.-G. Tseng, *J. Phys. Chem. C*, 2011, **115**, 16258.
29 E. Garnett and P. Yang, *Nano Lett.*, 2010, **10**, 1082.
30 C.-M. Hsu, S. T. Connor, M. X. Tang and Y. Cui, *Appl. Phys. Lett.*, 2008, **93**, 133109.
31 J. Zhu, C.-M. Hsu, Z. Yu, S. Fan and Y. Cui, *Nano Lett.*, 2010, **10**, 1979.
32 D.-G. Choi, H. K. Yu, S. G. Jang and S.-M. Yang, *J. Am. Chem. Soc.*, 2004, **126**, 7019.
33 C.-J. Heo, S.-H. Kin, S. G. Jang, S. Y. Lee and S.-M. Yang, *Adv. Mater.*, 2009, **21**, 1726.
34 C. X. Cong, T. Yu, Z. H. Ni, L. Liu, Z. X. Shen and W. Huang, *J. Phys. Chem. C*, 2009, **113**, 6529.
35 C. Haginoya, M. Ishibashi and K. Koike, *Appl. Phys. Lett.*, 1997, **71**, 2934.
36 Y. Li, J. Pan, P. Zhan, S. Zhu, N. Ming, Z. Wang, W. Han, X. Jiang and J. Zi, *Opt. Express*, 2010, **18**, 3546.
37 P. Zhan, Z. Wang, H. Dong, J. Sun, J. Wu, H.-T. Wang, S. Zhu, N. Ming and J. Zi, *Adv. Mater.*, 2006, **18**, 1612.
38 C. Tang, Z. Wang, W. Zhang, S. Zhu and N. Ming, *Phys. Rev. B: Condens. Matter Mater. Phys.*, 2009, **80**, 165401.
39 T. F. Krauss, *J. Phys. D: Appl. Phys.*, 2007, **40**, 2666.
40 Q. Gan, Z. Fu, Y. J. Ding and F. J. Bartoli, *Phys. Rev. Lett.*, 2008, **100**, 256803.
41 K. L. Tsakmakidis, A. D. Boardman and O. Hess, *Nature*, 2007, **450**, 397.
42 United State Environmental Protection Agency (US EPA) official website, http://www.epa.gov/pesticides/factsheets/chemicals/methyl.htm.
43 Agency for Toxic Substances and Disease Registry, http://www.atsdr.cdc.gov/toxprofiles/tp48-c7.pdf.
44 J. F. Li, Y. F. Huang, Y. Ding, Z. L. Yang, S. B. Li, X. S. Zhou, F. R. Fan, W. Zhang, Z. Y. Zhou, D. Y. Wu, B. Ren, Z. L. Wang and Z. Q. Tian, *Nature*, 2010, **464**, 392.
45 J. Wang, L. T. Kong, Z. Guo, J. Y. Xu and J. H. Liu, *J. Mater. Chem.*, 2010, **20**, 5271.

 This journal is © The Royal Society of Chemistry 2013